ACS NANO

www.acsnano.org

ARTICLE

# Stretchable and Directly Patternable Double-Layer Structure Electrodes with Complete Coverage

Junsung Bang, Junhyuk Ahn, Jinyuan Zhang, Tae Hee Ko, Byeonghak Park, Yong Min Lee, Byung Ku Jung, Sang Yeop Lee, Jehyung Ok, Bong Hoon Kim, Tae-il Kim, Jong-Il Choi,* Chi Hwan Lee,* and Soong Ju Oh*

Cite This: *ACS Nano* 2022, 16, 12134–12144

Read Online

ACCESS | Metrics & More | Article Recommendations | Supporting Information

**ABSTRACT:** **Stretchable electrodes are widely used in next-generation wearable electronics. Recent studies incorporated designs that help rigid electrodes attain stretchability. However, these structures exhibited unsatisfactory charge/signal extraction efficiency because of their low areal fill factor. Additionally, they cannot be photolithographically patterned on polymer substrates because of their low adhesion, requiring additional complicated fabrication steps. We developed photolithographically patternable stretchable electrodes with complete coverage and enhanced charge-extraction efficiency. The electrodes, comprising double layers, included a chemically treated Ag nanowire mesh and Au thin film. The interfacial linker role of polyvinylpyrrolidone chemically strengthened the interfacial bonds, and the reinforced concrete structure of nanowire-embedded metal thin films enhanced the mechanical properties. Therefore, the electrodes provided superior efficiency and stability in capturing physical, electromagnetic, and electrophysiological signals while exceeding the existing stretchable electrode limits. A broad range of applications are foreseen, such as electrocardiogram sensing electrodes, strain sensors, temperature sensors, and antennas.**

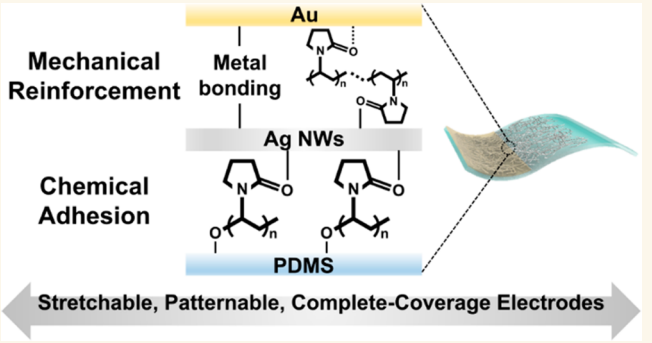


**KEYWORDS:** *direct patternable, stretchable electrode, complete coverage, adhesion, double-layer structure*



## INTRODUCTION

Stretchable electrodes have been spotlighted because they are used in numerous wearable electronic devices, such as Internet-of-things (IoT) sensors,[1−4] medical and health care devices,[5−9] textiles for electronic skins,[10−13] and human−robotic interactions.[14,15] Various functional materials have been investigated to produce stretchable electrodes without significantly compromising their mechanical and electrical properties during stretching. Extended studies have focused on the development of efficient, robust, stretchable, and conductive electrodes.[16−21] Recent studies concerning the development of stretchable electrodes are classified according to the material type. Organic electrodes[22] are intrinsically stretchable; however, their electrical conductivity is lower than that of inorganic electrodes. Inorganic electrodes[23,24] have been used following additional fabrication steps to incorporate stretchable designs such as serpentine fractals[2,3] and open meshes.[25−27] Despite the great advances in the field, two major drawbacks remain to be solved.

First, the inorganic stretchable electrodes exhibit unsatisfactory charge-extraction efficiency owing to the low areal fill factor (*i.e.*, surface area coverage, which is typically less than 15%) of their serpentine fractals[2,3] and open mesh designs.[25−27] The area of the electrode is compromised to disperse the strain and obtain a high stretchability. This characteristic is particularly problematic in optoelectronic devices and biosensors.[28−30] Specifically, optoelectronic devices, such as light-emitting diodes and solar cells, require electrodes with a high areal fill factor to enhance the charge-extraction efficiency (*i.e.*, external quantum and power conversion efficiencies). Additionally, biosensors require a

Received: March 17, 2022
Accepted: July 21, 2022
Published: August 4, 2022

**Scheme 1. (A) Proposed Design of Ag NW and Au Hybrid Thin-Film-Based Stretchable Electrodes and (B) Fabrication Process of Ag NW and Au Hybrid Thin Film Stretchable Electrodes**

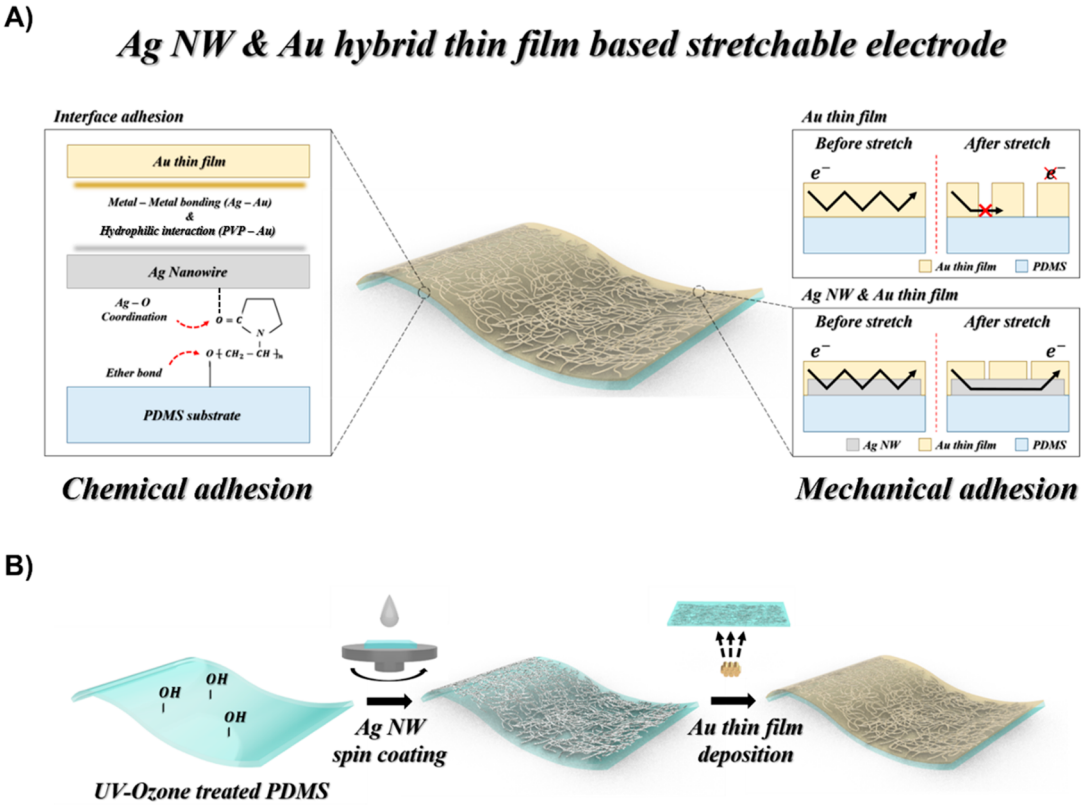


sufficiently large areal fill factor to extract electrophysiological signals accurately for applications such as obtaining an electrocardiogram (ECG), electroencephalogram, and electromyogram *via* skin contact. Thus, a complete-coverage technique must be developed to overcome these limitations.

Second, the photolithographic patterning of stretchable designs, such as serpentine fractals and open meshes, remains a challenge, particularly for highly stretchable elastomers, such as polydimethylsiloxane (PDMS), polyurethane, and Eco-flex. These elastomers exhibit a high surface chemical stability, resulting in low adhesion with photoresist and metal thin films. Consequently, it is challenging to coat the photoresists on these elastomers uniformly or to process the deposited metal thin films without incurring delamination. An alternative approach incorporates the transfer printing[3,29] of prepatterned conducting materials onto elastomers; however, securing the interfacial adhesion is a challenge, particularly when significant stretching is applied. Thus, another approach must be developed to overcome these limitations and directly pattern the stretchable electrodes onto elastomers with a 100% areal fill factor.[31]

In this study, we present a strategy to enhance the interlayer adhesion structural integrity of stretchable electrodes, which were developed on a PDMS substrate. The electrodes were composed of double layers of polyvinylpyrrolidone (PVP)-treated Ag nanowire mesh and Au thin film. This structure has chemically enhanced adhesion between the substrates and the electrode, developed by introducing PVP, a chemical linker that allowed for direct photolithographic patterning to occur without delamination. Additionally, it showed mechanically improved adhesion in intralayers by designing the reinforced concrete structure[32,33] inspired Ag nanowire (NW)+Au thin film hybrid layers, which lead to high stretchability, a low gauge factor, and a high areal fill factor. Utilizing these chemically and mechanically enhanced stretchable electrodes, the electrodes exhibited a complete areal fill factor (100%), charge-extraction efficiency (~100%), stretchability (>100%, with a low gauge factor < 10), and photolithographic patternability with a minimum feature size of 5 $\mu$m. The functionality of these electrodes was demonstrated in biosensors, antenna, and pressure, strain, and temperature gauges. We envision that our stretchable electrodes will be useful for many stretchable electronics.[34−37]

## RESULTS AND DISCUSSION

This study investigates the development of high-efficiency, high-performance stretchable electrodes capable of patterning. The key elements required for improving the patternability and stretchability of the electrodes are (i) chemical adhesion between the interlayers and (ii) mechanical adhesion between the intralayers. The proposed design for the hybrid thin film stretchable electrodes having chemically treated Ag NW mesh and Au thin films with a 100% areal fill factor is as follows (Scheme 1A). First, the chemical adhesion is of importance because the intrinsically low adhesive surface of the stretchable polymer does not allow subsequent fabrication processes. Therefore, the hydrophobic surface of PDMS was modified into a hydrophilic surface through UV-ozone treatment[38,39] to make the surface reactive and enhance the adhesion of Ag NW thin films through PVP as an interfacial link material. The PVP is used as a linker material for the following reasons: (i) PVP combines with the −OH group on the surface of the PDMS substrate, and ether bonds (PDMS−O−PVP, R−O−R′) are formed after annealing at 150 °C.[40] The binding energy of C


https://doi.org/10.1021/acsnano.2c02664
ACS Nano 2022, 16, 12134−12144

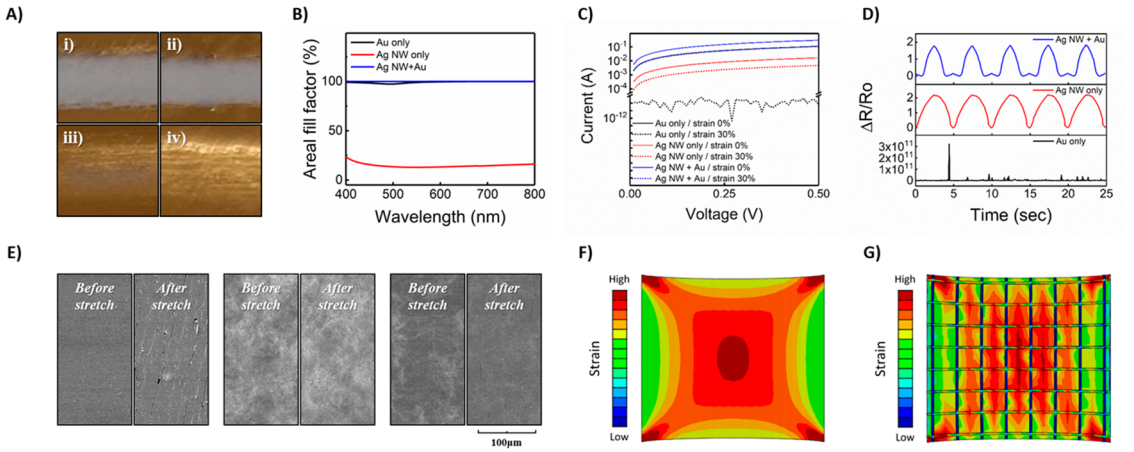


**Figure 1. (A) Adhesion test data of (i) Au only, (ii) Ag NW+Au, (iii) PVP+Au, and (iv) PVP+Ag NW+Au electrode surfaces scratched using a cotton swab. (B) Areal fill factor data of Au only (black), Ag NW only (red), and Ag NW+Au (blue) thin films on PDMS substrate. (C) *I*–*V* characteristics of Au only (black), Ag NW only (red), and Ag NW+Au (blue) thin films on PDMS substrate at $\varepsilon$ = 0% (solid) and $\varepsilon$ = 30% (dot). (D) Relative resistance change of Au only (black), Ag NW only (red), and Ag NW+Au (blue) thin films on PDMS substrate when 0–30% strain cycles were applied. (E) Surface SEM images of Au only thin films (left), Ag NW only thin films (middle), and Ag NW+Au thin films (right) before and after stretching. (F) FEM simulation data of Au only thin films under 10% stretching condition. (G) FEM simulation data of Ag NW+Au thin films under 10% stretching condition.**

1s for the C–O–C bond is ~288 eV.[41,42] (ii) The high-surface-energy (100) plane of Ag NWs can be passivated through Ag:O coordination. This coordination anchors PDMS substrates and Ag NWs by forming PDMS–O–PVP–Ag linkage. In addition, the interface between Ag NWs and Au showed high adhesion because the Ag $3d^{5/2}$ in the Ag–Au bond has a high binding energy of ~368 eV owing to the default metal (hydrophilic)–metal (hydrophilic) interaction.[43] Additionally, the O present in the pyrrolidone ring of PVP bonded *via* Ag:O coordination[44−46] on the surface of the Ag NWs form the hydrophilic interactions with Au, thus improving the Ag NWs and Au adhesion further. This theoretical approach has been investigated experimentally using XPS spectroscopy. The 286.25 eV peak was observed in the PVP treated PDMS, which corresponds to the C–O–C bond.[41] In addition, a significant shift (0.875 eV) in the O 1s binding energy was observed, which was attributed to the fact that the electron density of O atoms in PVP decreased, implying the existence of Ag:O coordination.[44] (Figure S1). Therefore, PVP chemically improved the Ag NW+Au thin film electrodes interface adhesions and prevented the electrode delamination.

Second, the mechanical adhesion is important because stretchability is achieved by ensuring sufficient mechanical strength when the electrode expands. Therefore, an Ag NW +Au thin film that imitated a reinforced concrete structure was designed to develop high-performance stretchable electrodes through a mechanical adhesion enhancement strategy. To implement this structure, the Ag NWs acts as the rebar and provide high stretchability, and the Au acts as the concrete and has 100% areal fill factor. In this way, the Ag NW thin films were expected to resolve the crack formation caused by the low stretchability characteristic of the Au thin films; the Au thin films were expected to solve the low charge-extraction efficiency problem caused by the low areal fill factor of the Ag NW thin films. Additionally, the interlayer adhesion was improved mechanically by the reinforced concrete structure of the Ag NW+Au double-layer structure. Through increased adhesion, the double-layer thin films prevented the electrode delamination and surface crack formation and provided an electron path by connecting between the cracks.

The fabrication process of the stretchable electrodes is shown in Scheme 1B. The PDMS substrate was prepared by mixing a base and curing agent in a 10:1 ratio, spin-coating it to the desired thickness, and annealing at 70 °C for 1 h. At this time, the thickness of the PDMS substrate could be adjusted from 100 $\mu$m to ~mm. The UV-ozone treatment was conducted on the surface to facilitate the subsequent processes and reduce the surface chemical stability by forming –OH on the surface (see the Discussion and Figure S2 in the Supporting Information). Subsequently, the Ag NWs were synthesized and dispersed in ethanol.[47] Thereafter, PVP was added to increase adhesion with the PDMS surface. The Ag NWs and PVP dispersed in ethanol were spin-coated at 1000–3000 rpm to form thin films, and nanowire network mesh structures were formed. Finally, Au thin films with a thickness of 50–200 nm and an 100% areal fill factor were formed *via* thermal deposition to fabricate highly stretchable, high-efficiency electrodes (see the Discussion and Figure S3 in the Supporting Information).

The effects of chemical and mechanical adhesion enhancements were examined. To verify the adhesion enhancement of PVP and Ag NWs, adhesion tests were conducted under (i) Au only, (ii) Ag NW+Au, (iii) PVP+Au, and (iv) PVP+Ag NW +Au electrode conditions (Figure 1A). The adhesion test was conducted by scratching the surfaces of the thin films with a cotton swab at a pressure of $3.27 \times 10^5$ Pa. (i) and (ii) showed completely delaminated surfaces, and (iii) exhibited slightly delaminated surfaces, but the delamination was less than that for (i) and (ii). In contrast, (iv) indicated scratched traces but not delaminated surfaces. To compare these results quantitatively, we converted Figure 1A to pixels, and analyzed the degree of delamination by dividing the delaminated pixels by the total number of pixels (Figure S4A). The degree of delamination of (i) and (ii) is 99% and that of (iii) and (iv) is 8% and 1%, respectively. To support the degree of delamination clearly, the transmittance at 550 nm wavelength of the visible light was measured for i–iv, and the results are


https://doi.org/10.1021/acsnano.2c02664
ACS Nano 2022, 16, 12134–12144

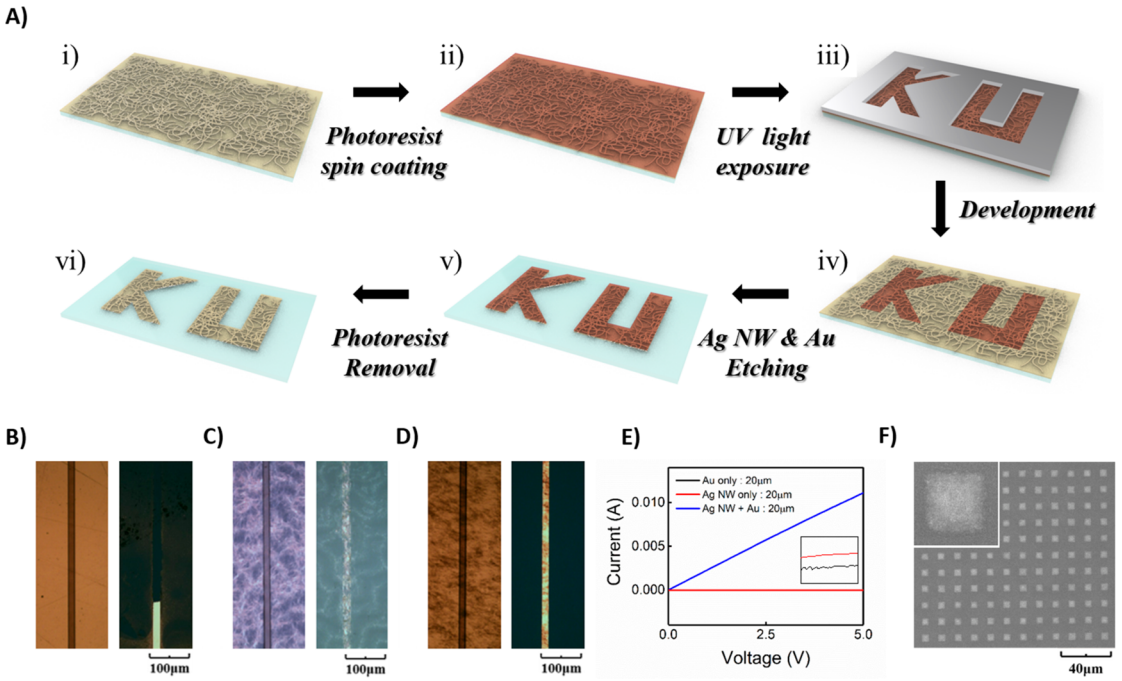


**Figure 2. (A) Patterning/etching of a double-layer electrode. (B–D) Optical microscope images of Au only (B), Ag NW only (C), and Ag NW+Au (D) in step (iv) (left) and (vi) (right) with a 20 $\mu$m pattern. (E) $I$–$V$ characteristics of Au only (black), Ag NW only (red), and Ag NW+Au (blue) after the patterning/etching process. (F) SEM images of a 5 $\mu$m × 5 $\mu$m array pattern.**

shown in Figure S4B. The transmittance was 96%, 90%, 7.6%, and 1.5%, for (i), (ii), (iii), and (iv), respectively, indicating that the calculation method for estimating the degree of delamination was reasonable. Consequently, these results confirmed the improvement in the adhesion of PVP and Ag NWs. Then, a solvent test was conducted by washing thin films in several solvents, shown in Figure S5. These results confirmed the adhesion enhancement effect of PVP in the double-layer structure designed in this study. Since the adhesion was enhanced when the Ag NW solution was used with PVP, all the subsequent experiments were conducted with PVP.

To investigate the areal fill factor of the thin films, an optical spectroscopy analysis was conducted in the range of 400–800 nm (Figure 1B). The areal fill factor was extracted using transmittance spectra because visible light cannot be transmitted through the area covered by the electrodes. The Au only (black) and Ag NW+Au (blue) thin films showed nearly a 100% areal fill factor, whereas the Ag NW only (red) thin films only showed an average areal fill factor of 20%.

The electrical and electromechanical properties of Ag NW +Au thin film electrodes were examined to confirm their stretchability and conductivity under strain conditions. In Figure 1C, $I$–$V$ curves for Au only (black), Ag NW only (red), and Ag NW+Au (blue) thin films on the PDMS substrate are investigated with ($\varepsilon$ = 30%, dot) and without ($\varepsilon$ = 0%, solid) stretching conditions. In the case of 0.5 V with $\varepsilon$ = 0%, the current of Au only (black), Ag NW only (red), and Ag NW +Au (blue) were $1.12 \times 10^{-1}$, $1.66 \times 10^{-2}$, and $3.04 \times 10^{-1}$ A, respectively. In the case of 0.5 V with $\varepsilon$ = 10%, the current of each sample was measured as $6.69 \times 10^{-11}$, $4.75 \times 10^{-3}$, and $1.06 \times 10^{-1}$ A, respectively. The current change upon a stretching condition, $\varepsilon$ = 0%, 10%, 20%, and 30% at 0.5 V; these cases were analyzed for comparison (Figure S6). In the case of Au only (black), the current decreased excessively, up to $10^9$ times after 10% stretching, indicating that cracks were formed. Conversely, Ag NW only (red) and Ag NW+Au (blue) showed a small decrease in current after 30% stretching. The current of Ag NW only and Ag NW+Au decreased from $1.66 \times 10^{-2}$ and $3.04 \times 10^{-1}$ A to $4.75 \times 10^{-3}$ and $1.06 \times 10^{-1}$ A, respectively. The gauge factor was calculated from these results using eq 1:

$$\text{Gauge Factor} = (\Delta R/R_0)/\varepsilon \quad (1)$$

where $R_0$, $\Delta R$, and $\varepsilon$ are the initial resistance, resistance change, and strain, respectively. The gauge factors of Au only, Ag NW only, and Ag NW+Au were extracted as $5.6 \times 10^9$, 8.32, and 6.22, respectively.

Finally, 0–30% strain cycle tests were analyzed at 0.5 V (Figure 1D). Similar to the previous results, Au only (black) showed unstable, unreliable cycle curves. Ag NW only (red) showed a stable, reliable cycle curve; however, it had a low current and areal fill factor. In contrast, the relative resistance change has been minimized for Ag NW+Au (blue) and showed a stable, reliable cycle curve. Additionally, the Ag NW+Au electrode with a high areal fill factor exhibited high conductivity, stable behavior, and excellent charge-extraction efficiency. This could be confirmed quantitatively from the luminance-areal fill factor plot (see the Discussion and Figure S7 in the Supporting Information).

The surface and structure of each sample were examined by scanning electron microscopy (SEM) analysis to understand the electromechanical behavior (Figure 1E). In the case of Au only, a microsize crack, ~3 $\mu$m width and ~300 $\mu$m length, was formed across the surface area after stretching, as seen in Figure 1E,left. Conversely, Ag NW only showed no structural change after stretching (Figure 1E,middle), and Ag NW+Au formed infrequent cracks, 1 $\mu$m width and 30 $\mu$m length on the surface after stretching (Figure 1E,right). To investigate the cause of the different surface crack sizes and densities, the finite


https://doi.org/10.1021/acsnano.2c02664
ACS Nano 2022, 16, 12134–12144

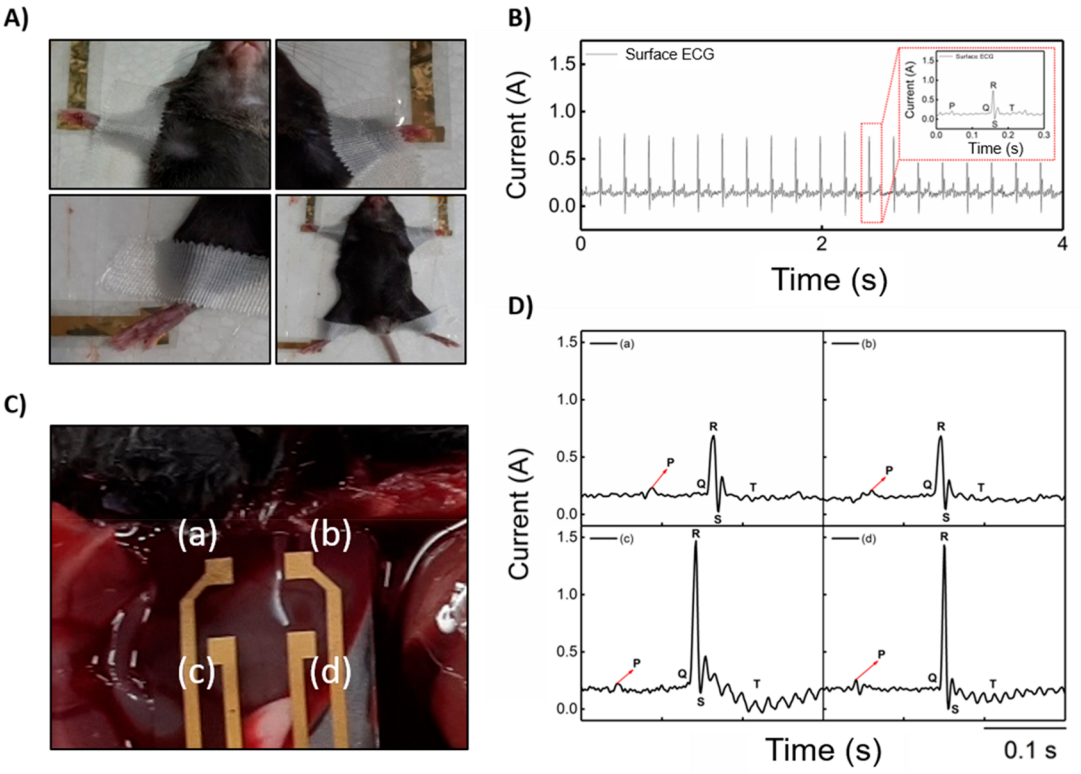


**Figure 3. (A) Surface electrocardiogram (ECG) performed by a placing stretchable electrode on the forelimb (left and right) and hindlimb (left). (B) Representative data of the surface ECG of 8-week mice. (C) Photograph of a 2 × 2 array electrode for ECG recoding of the exposed mouse heart. (d) Representative data of each location of the 2 × 2 array electrodes from an exposed mouse heart.**

element method (FEM) simulation was conducted (Figure 1F,G). Strain changes were monitored under stretching the thin films. The results of the FEM simulation showed that the strain was concentrated at the center of the Au only thin films (Figure 1F). In contrast, the concentrated strain was dispersed onto the entire substrate forming a low strain region adjacent to Ag NWs in the Ag NW+Au thin films (Figure 1G). These results were attributed to the reinforced concrete structure of the Ag NW+Au thin films. When an external strain was applied to Ag NW+Au thin films, the embedded Ag NWs acted in a similar fashion to that of rebar, to resist the external strain, and the mesh structure of the Ag NWs dispersed the external strain applied to the Au thin films. Additionally, the strain dispersing effect of the reinforced concrete structure prevented the formation of the microsized cracks on the surface and the destruction of the electrodes. Furthermore, a 3D view of the FEM simulated sample is shown in Figure S8. Consequently, the reinforced concrete structure improved the mechanical properties of the Ag NW+Au double-layer thin film electrodes.

In Figure 2A, the direct photolithography process was conducted on Ag NW+Au thin film stretchable electrodes with improved adhesion; the process is as follows: (i) the photoresist (GXR 601) was spin-coated onto the Ag NW +Au thin film electrodes and baked at 100 °C. (ii) Thereafter, the sample was exposed to UV light using the desired photomask pattern. (iii) The sample was developed with the developer and rinsed with deionized (DI) water to complete the patterning process. (iv) Finally, the etching process was completed using potassium monoiodide (DI base), and a lift-off with acetone was conducted.

A comparative analysis to confirm the results of the patterning/etching process was conducted. The optical microscope images of Au only, Ag NW only, and Ag NW +Au thin film electrodes before etching (left image, corresponding to step iv of Figure 2A), and after etching and PR removal (right image, corresponding to step vi of Figure 2A) processes are shown in Figure 2B–D. In the case of Au only, a neat PR pattern was obtained before etching; however, delamination occurred after etching and PR removal (Figure 2B). In the case of Ag NW only, a neat PR pattern was obtained; however, a blurred noncontinuous pattern formed after etching and PR removal (Figure 2C). Conversely, in the case of Ag NW+Au thin films, a neat PR pattern was obtained, which remained stable after etching and PR removal (Figure 2D). The Au only thin film delamination after etching and PR removal was caused by low adhesion between the PDMS substrate and Au thin films. During the etching and PR removal, the etchant penetrates into the interface between the PDMS substrate and Au thin films and peeled off the Au thin films. The PR removal solvent then washed off the remaining patterned Au thin films. In the case of Ag NW only thin films, the etchant readily penetrates into the interface between PR and PDMS because of their low adhesion, thus leading to incomplete pattern formation (see the Supporting Information, Figure S9). However, in the case of Ag NW+Au thin films, strong adhesion occurred because of ether bonding and the Ag:O coordination between PDMS and Ag NWs as well as the metal–metal bonding between Ag NWs and the Au thin films. The improved adhesion prevented the electrode delamination during the etching and PR removal processes and helped fabricate the patterned electrodes.

The electrical property of the patterned/etched thin film was analyzed with $I-V$ characteristics (Figure 2E). The Au only and Ag NW only thin film electrodes showed currents of $10^{-13}$


https://doi.org/10.1021/acsnano.2c02664
ACS Nano 2022, 16, 12134–12144

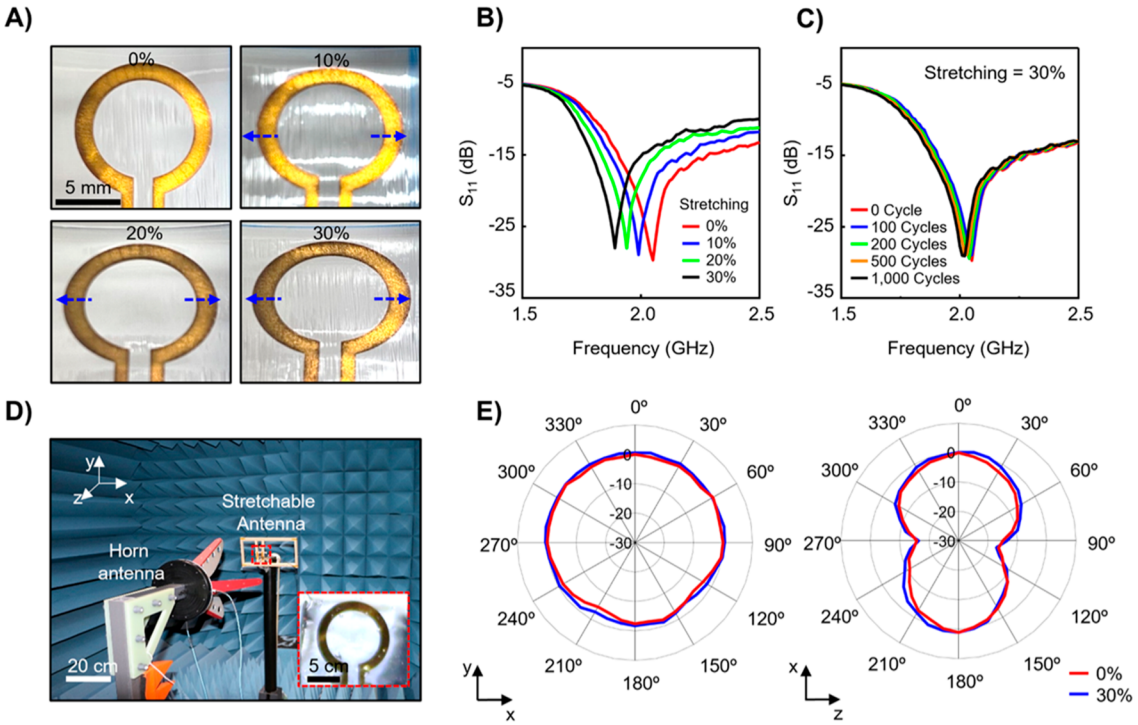


**Figure 4. (A) Photographs of the antenna under stretching. (B) Return loss ($S_{11}$) spectra of the antenna under stretching up to 30%. (C) Return loss ($S_{11}$) spectra of the antenna under up to 1 000 cycles of repeated stretching at 30%. (D) Experimental setup for radiation pattern measurement in the anechoic chamber. (E) Radiation pattern of the antenna under stretching at 0% and 30% in the *x*−*y* (left panel) and *x*−*z* (right panel) planes, respectively.**

and $10^{-11}$ A, respectively, indicating that the patterning failed and that these electrodes were inappropriate for use. In contrast, the Ag NW+Au thin film electrode showed a current of 0.011 A, corresponding to a resistivity of $3.64 \times 10^{-8}$ Ω m. Various patterns were successfully fabricated with a minimum feature size of 5 $\mu$m (Figure 2F and Figure S10); additionally, the stretchability was confirmed through stretching, tilting, and bending tests (Figure S11). Consequently, it was confirmed that the chemically and mechanically enhanced Ag NW+Au thin films were applicable as appropriate patterned/etched stretchable electrodes. The comparison of recent stretchable electrodes shows that our stretchable electrodes exhibit outstanding performance (Table S1).

The double-layer thin film stretchable electrodes manufactured through the preceding patterning/etching process showed high conductivity, stretchability, and chemical/mechanical stability. These characteristics are advantageous in various fields, such as healthcare systems. For example, high conductivity and stretchability are key factors for high detectivity owing to a stable conformal contact with the skin. To demonstrate the electrode performance, ECG sensor arrays were fabricated and examined *in vivo*.[48]

As shown in Figure 3A, the ECG measurements were performed on the external surface of a mouse. The 3-lead ECG measurement method was adopted, which measured the body signals by attaching the electrodes to the forelimb and hindlimb of a mouse. A 5 mm size patterned electrode showed the ECG signals of a mouse; each signal was monitored separately (Figure 3B). The beating rate was 4.25 beats/s; the P, Q, R, S, and T waves are shown in Figure 3B. The (P), (Q-R-S), and (T) waves indicated the occurrence of atrial and ventricular depolarization as well as ventricular repolarization, respectively.

Additionally, the ECG measurements were conducted on the exposed heart of the mouse to detect its heartbeat. The 2 × 2 electrode arrays were attached directly to the surface of the heart (Figure 3C). Each of the electrodes in the array was used as a cathode, and the needle-shaped electrodes were used as the anode and ground. All the electrodes were combined to form 3-lead electrodes (Figure S12). Each electrode showed a conformal contact with the 5 mm × 5 mm rodent heart. To minimize the interference between the array electrodes measuring the ECG signals at different locations, 1 × 1 $mm^2$ electrodes spaced at 2 mm were fabricated. Each electrode location was labeled as (a), (b), (c), and (d) to avoid mixing up the ECG signals. The currents of ECG signal at each location of the array are shown in Figure 3D. Similar to the heart waves provided by the surface ECG measurements, the ECG sensors displayed distinct P, Q, R, S, and T waves at each location of the exposed mouse heart. The difference in the generated current at different locations of the electrode was confirmed, proving that the amount of current produced depends on the electrode length. However, this alteration of the generated current was negligible because the waveforms of the ECG signals are independent of the amount of the generated current. This signifies that the double-layer thin film stretchable electrodes could be applied to *in vivo* ECG measurements and display high device performance for healthcare systems.

In Figure 4A, a stretchable microwave antenna[1,4] was enabled by directly patterning the double-layer thin film stretchable electrodes into a ring shape with inner and outer diameters of 8 and 11 mm, respectively. The antenna was stretched up to 30%, without mechanical failure. Figure 4B shows the return loss ($S_{11}$) spectra of the antenna for stretching up to 30% using a vector network analyzer (VNA;


https://doi.org/10.1021/acsnano.2c02664
ACS Nano 2022, 16, 12134−12144

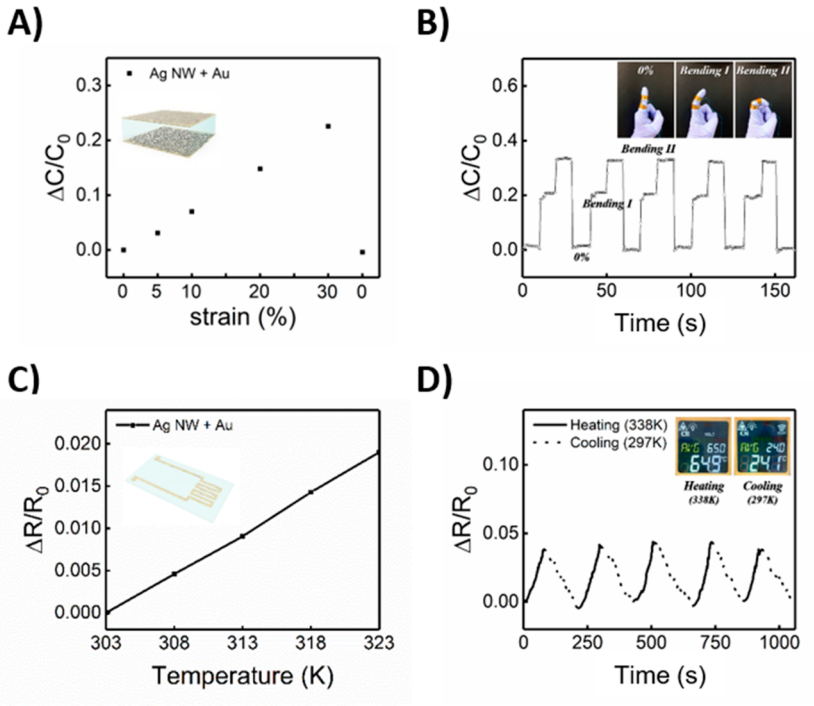


**Figure 5. (A) Capacitance of a stretchable strain sensor when strain was applied. (B) Relative capacitance change of a stretchable strain sensor when bending was applied. (C) Relative resistance change of a temperature sensor at 303, 308, 313, 318, and 323 K. (D) Demonstration of the temperature sensor.**

Field Fox Hand-held Analyzer 9913A, Keysight Technologies Inc.). The resonant frequency of the antenna decreased slightly from 2.05 to 1.89 GHz when stretched from 0 to 30%. Because the deformation of the antenna led to an increase in its inductance and capacitance, which in turn decreased the resonant frequency. Such a shift in the resonant frequency is in good agreement with a previous study.[49] The resonant frequency barely shifted to <0.018 GHz after 1 000 stretching cycles at 30% (Figure 4C). The far-field radiation pattern of the antenna was characterized by unstretched (0%) and stretched (30%) conditions at their resonant frequencies in an anechoic chamber (Figure 4D). Figure 4E presents the 2-dimensional (2D) polar plots of the radiation pattern of the antenna under 0 and 30% stretching in the $x-y$ (left panel) and $x-z$ (right panel) planes. The radiation pattern of the antenna barely changed under stretching, and the gain remained at approximately 0 dB. Consequently, the antenna retained its essential properties under stretching in terms of resonant frequency, radiation pattern, and gain, which confirmed the mechanical and electrical reliability of the double-layer thin film stretchable electrodes.

A capacitive-type strain sensor, pressure sensor, and resistive-type temperature sensor were fabricated. The sandwich structures were manufactured with a PDMS layer having top and bottom double-layer thin film stretchable electrodes, to fabricate capacitive-type strain and pressure sensors. In the wearable capacitive-type sensors, the stretchable electrode plays an important role as it should reliably deliver the capacitances of PDMS to external circuits even under bending or stretching. The manufactured sensor detected the applied strain and pressure based on the changes in capacitance, which varied according to the changes in the thickness of the PDMS substrate. When the device was stretched, the thickness decreases upon the Poisson's ratio, causing a capacitance change. The sensitivity of the capacitive-type strain sensor was defined as the capacitive gauge factor, which was different from the gauge factor of the resistance-type strain sensor and was calculated using eq 2:

$$S_s = \frac{\Delta C/C_0}{\varepsilon} \tag{2}$$

where $S_s$, $\Delta C$, $C_0$, and $\varepsilon$ are the sensitivity of the capacitive-type strain sensor, capacitance change, capacitance without strain, and applied strain, respectively.

A stretching test was conducted to investigate the sensitivity under strain conditions (Figure 5A). The relative capacitance changes were 0.0311, 0.0701, 0.1479, and 0.2257 at strains of 5%, 10%, 20%, and 30%, respectively; the relative capacitance change became approximately zero when stretching was released. The sensitivity of the capacitive-type strain sensor was 0.703 ± 0.051, showing a tendency for full recovery after stretching. To demonstrate strain detection, a bending test was conducted by attaching a strain sensor to a finger (Figure 5B). The relative capacitance cycles of the initial state(without bending), the bending I (bending 32°), and bending II (bending 55°) states were analyzed. An equivalent relative capacitance change was recorded in each state, and the real-time monitoring capability was confirmed. Furthermore, the stretching recyclability of stretchable electrodes is shown in Figure S13, which shows a fully recovered current after 1000 times of 0% to 10% stretching, that could be used as electrodes of capacitive-type sensors was confirmed. This sandwich structured capacitive-type sensor could use as also a pressure sensor (see the Discussion and Figure S14 in the Supporting Information).

Then, a temperature sensor was fabricated using a low gauge factor of Ag NW+Au thin films. The sensitivity of the


https://doi.org/10.1021/acsnano.2c02664
ACS Nano 2022, 16, 12134−12144

temperature sensor was calculated using the temperature coefficient of resistance, as shown in eq 3:

$$\mathrm{TCR} = (\Delta R/R_0)/\Delta T \quad (3)$$

where $\Delta R$, $R_0$, and $\Delta T$ are the resistance change, initial resistance, and temperature change, respectively.

The temperature variable electrical measurements were conducted at 303 and 323 K (Figure 5C and Figure S15A). As the temperature increased, the resistance increased linearly, and the sensitivity was calculated as $9.51 \times 10^{-4}$ $K^{-1}$. The cycle test showed stable and reliable behavior, as shown in Figure S15B. To investigate the stretching noninterference characteristics of a temperature sensor, electrical measurements, and cycle tests at 303 and 323 K were conducted under stretched conditions. After stretching, the resistance increased linearly, similar to the nonstretched condition, and the sensitivity showed an almost equivalent value of $9.76 \times 10^{-4}$ $K^{-1}$, with a 2.6% deviation (Figure S16A). The cycle test showed reliable properties, as shown in Figure S16B. To confirm the real-life performance of the temperature sensor, the temperature change of the fan heater was measured. The temperature sensor was placed on the fan heater, and the relative resistance change was investigated through heating and cooling (Figure 5D). The temperature change, measured with an IR detector, was from 297.1 to 337.9 K, and the temperature change calculated by the temperature sensor was 40.69 K. The temperature sensor measurement error was 0.11 K; thus, the real-life temperature sensing capability and accuracy were confirmed.

## CONCLUSION

In this study, we developed complete-coverage, high-performance, high-efficiency, and directly patternable stretchable electrodes. An interfacial layer adhesion investigation was conducted, and the adhesion was improved using a chemical adhesion enhancement strategy with PVP as the linking material and a mechanical adhesion enhancement strategy with a double-layer structure inspired by a reinforced concrete structure. The results of these adhesion enhancement strategies were demonstrated through FEM simulations and electric and electromechanical analyses. Further, we developed ECG sensing electrodes, strain sensors, temperature sensors, and antenna devices based on double-layer thin film stretchable electrodes. Our approach to the adhesion enhancement strategy provides key information for fabricating wearable devices, and we believe that the proposed double-layer thin film stretchable electrodes could be a source technology for the development of healthcare monitoring, e-skin, and robotics.

## EXPERIMENTAL SECTION

**Materials.** Silver nitrate ($AgNO_3$, 99.9+%), iron(III) nitrate nonahydrate ($Fe(NO_3)_3$, 98+%), 1-octadecene (ODE, 90%), and tetramethylammonium hydroxide (TMAH) were purchased from Alfa Aeser, Co. 1,2-Dodecanediol (DD, 90%), sodium chloride (NaCl, ≥99.5%), isopropanol (IPA, 99.5%), ethylene glycol (EG, 99.8%), acetone (≥99.5%), ethanol (≥99.5%), PVP (average Mw ~ 55 000), AZ GXR 601 (46 cP), MIF 300 K (TMAH aqueous solution), gold etchant, oleic acid (OA, 90%), dimethyl sulfoxide (DMSO, ≥99.9%), cadmium acetate hydrate ($Cd(AC)_2{\cdot}2H_2O$, ≥99.99%), zinc acetate dehydrate ($Zn(AC)_2{\cdot}2H_2O$, ≥98%), zinc oxide (ZnO, ≥99.0%), ethyl acetate (99.8%), 2-ethanolamine (≥99.5%), selenium (99.99%), sulfur (99.998%), and 2,2,2-tribromoethanol (avertin) were obtained from Sigma-Aldrich Co. Trioctylphosphine (TOP, 90%) was obtained from Acros Organics Co. PDMS (Sylgard 184 silicone elastomer kit) was purchased from the Dow Corning Corporation. Propylene glycol (PG, >99.0%) was obtained from Samchun Co. ITO glass was purchased from AMG Co. (Tokyo, Japan). Poly(3,4-ethylenedioxythiophene):poly(styrenesulfonate) (PEDOT:PSS, Al4083) was purchased from Ossila Co. All the reagents were used without further purification.

**Synthesis of Ag Nanowires.** Ag NWs were synthesized based on a previously reported protocol;[47] 4 mL of PG was placed at room temperature. Thereafter, the EG-based $Fe(NO_3)_3$ solution (40 mM, 450 μL), NaCl solution (15.75 mM, 300 μL), and $AgNO_3$ (76.5 mg, 3.25 mL) were mixed with PG in a vial. After mixing, the reaction vial was heated to 180 °C, left for 5 min without stirring, and cooled in air to room temperature. The as-synthesized Ag NWs were diluted with IPA containing DD (5 wt %). Thereafter, it was centrifuged three times at 3000 rpm for 10 min with IPA and dispersed in IPA.

**Synthesis of ZnO Nanocrystals.** ZnO nanocrystals (NCs) were synthesized based on a previous report[50] with slight modifications; a 3 mmol $Zn(AC)_2{\cdot}2H_2O$ (dissolved in 30 mL of DMSO) solution was mixed with 5 mmol of TMAH (dissolved in 10 mL of ethanol) and stirred for 24 h under ambient conditions. Thereafter, the as-synthesized ZnO NCs were precipitated by adding ethyl acetate and centrifuged at 7000 rpm for 4 min. After centrifugation, the precipitated ZnO NCs were redispersed in ethanol and 160 μL of 2-ethanolamine was added to stabilize the solution.

**Synthesis of CdSe@ZnS Core–Shell.** A CdSe@ZnS core–shell was synthesized according to previous report protocols;[51] $Cd(AC)_2{\cdot}2H_2O$ (0.42 mmol), ZnO (10.23 mmol), and OA (21 mL) were mixed in a three-neck flask and degassed. After degassing, the mixture was heated up to 150 °C under a $N_2$ flow, ODE (45 mL) was added, and the mixture was heated to 310 °C. Thereafter, an anionic stock solution (6.6 mmol of Se and S dissolved in 6.6 mL of TOP) was rapidly injected, and the core reaction proceeded for 10 min. Subsequently, 4.8 mmol of S (dissolved in 7.2 mL of ODE) solution was introduced and held for 12 min. Thereafter, a Zn stock solution (8.58 mmol of $Zn(AC)_2{\cdot}2H_2O$ dissolved in 3 mL of OA and 12 mL of ODE) was injected and a S stock solution (28.95 mmol of S dissolved in 14 mL of TOP) was dropped into the mixed solution. Subsequently, ZnS shelling was conducted at 270 °C for 20 min.

**Substrate Preparation.** PDMS was used as the stretchable substrate in the experiments. The PDMS substrates were fabricated using the following procedure. The SYLGARD 184 silicone elastomer and curing agent were mixed at a ratio of 10:1 by weight. The PDMS mixture was spin-coated onto a Petri dish with a target thickness and heat at 70 °C for 12 h.

**Characterization.** UV–vis spectroscopy (JASCO, V-770) was used to characterize the transmittance spectra. The transmittance spectra were used to extract the areal fill factor because visible light cannot be transmitted through the covered area of the electrodes. The current–voltage, capacitance–voltage, and current–time analyses were conducted using a probe station (model MST-4000A, MSTECH), a semiconductor parameter analyzer (model 4156C, Hewlett-Packard), and a source meter (Keithley 2400, Tektronix), respectively. The surface characteristics were analyzed using scanning electron microscopy (High Technologies America Inc., Hitachi S-4300) and optical microscopy (MA200, Nikon).

**FEM Simulation.** FEM simulation was performed using commercial software (ABAQUS; CAE 6.13-1). The entire system was set to 2 μm (width) × 2 μm (thickness) × 240 μm (height) for comparison. The detailed dimensions were set with a thickness of Au at 60 nm, thickness of Ag at 20 nm, and a distance between the Ag NWs at 240 nm. The mechanical properties of Au, Ag NW, and PDMS were set at Young's moduli with 54 GPa, 87 GPa, and 700 kPa and Poisson's ratios of 0.44, 0.225, and 0.4, respectively. The $x$-direction of the strain was analyzed at 10% stretching.

**LED Characterization.** The LED fabrication process referred a previously reported protocol;[52] the PEDOT:PSS was spin-coated onto ITO glass and heated to 105 °C for 10 min. Thereafter, the CdSe@ZnS core–shell and ZnO were spin-coated and annealed at 180, 180, and 105 °C, respectively. To confirm the difference in charge-extraction efficiency between the Ag NW and Ag NW+Au


https://doi.org/10.1021/acsnano.2c02664
ACS Nano 2022, 16, 12134–12144

electrodes, light-emitting measurements were recorded. Each top electrode was deposited on the LED, and a voltage linear sweep was conducted using a source meter (Keithley 2400, Tektronix) at 0−6 V with 0.1 V increments.

**ECG Characterization.** For surface ECG recordings, 8-week old mice were anesthetized with 1.2% avertin. After the induction of anesthesia (<2 min), the anesthetized mice were placed in the supine position and electrodes were placed in the lead II position. The ECG recordings were performed in the following positions: (i) electrode placed on the right and left forelimbs as well as the left hindlimb and by fixing in position with tape or (ii) electrode placed on the exposed heart surface after the incision of the rib. ECG recordings were acquired using PowerLab 16/35 and analyzed using Labchart 8 (AD Instruments).

**Antenna Characterization.** The antenna was anchored on a wooden stretcher using Kapton tape and thereafter stretched up to 30% without mechanical failure. The spectra of the return loss ($S_{11}$) of the antenna were acquired in an anechoic chamber (ETS Lindgren Inc.) using a VNA (FieldFox Hand-held Analyzer 9913A; Keysight Technologies Inc.). The resonant frequency shift of the antenna was acquired under 100, 200, 500, and 1 000 cycles of stretching at 30%. The distance between the transmitting and receiving antennas was maintained at more than the Fraunhofer distance ($d$), to acquire the far-field radiation pattern:

$$d = \frac{2D^2}{\lambda} \tag{4}$$

where $D$ is the outer diameter of the stretchable antenna and $\lambda$ is the wavelength of the radio wave. The power received by the antenna before and after stretching at 30% was measured in both the $x-y$ and $x-z$ planes at their corresponding resonant frequency of 2.05 and 1.89 GHz, respectively. During the measurement process, the antenna was rotated 360° at intervals of 10° in each plane.

## ASSOCIATED CONTENT

### Supporting Information

The Supporting Information is available free of charge at https://pubs.acs.org/doi/10.1021/acsnano.2c02664.

Contact angle, SEM, optical images, $I-$strain curve, $I-V$ curve, and $R-T$ curve data (PDF)

## AUTHOR INFORMATION


### Corresponding Authors

**Soong Ju Oh** − *Department of Materials Science and Engineering, Korea University, Seoul 02841, Republic of Korea;* orcid.org/0000-0003-1434-8844; Email: sjoh1982@korea.ac.kr

**Chi Hwan Lee** − *Weldon School of Biomedical Engineering, School of Mechanical Engineering, School of Materials Engineering, and Brick Nanotechnology Center, Purdue University, West Lafayette, Indiana 47907, United States;* orcid.org/0000-0002-4868-7054; Email: lee2270@purdue.edu

**Jong-Il Choi** − *Division of Cardiology, Department of Internal Medicine, Korea University College of Medicine and Korea University Medical Center, Seoul 02841, Republic of Korea; Ion Channel Research Unit, Cardiovascular Research Institute, Korea University, Seoul 02841, Republic of Korea;* Email: jongilchoi@korea.ac.kr

### Authors

**Junsung Bang** − *Department of Materials Science and Engineering, Korea University, Seoul 02841, Republic of Korea;* orcid.org/0000-0002-0673-6700

**Junhyuk Ahn** − *Department of Materials Science and Engineering, Korea University, Seoul 02841, Republic of Korea;* orcid.org/0000-0003-0103-5080

**Jinyuan Zhang** − *Weldon School of Biomedical Engineering, Purdue University, West Lafayette, Indiana 47907, United States*

**Tae Hee Ko** − *Division of Cardiology, Department of Internal Medicine, Korea University College of Medicine and Korea University Medical Center, Seoul 02841, Republic of Korea; Ion Channel Research Unit, Cardiovascular Research Institute, Korea University, Seoul 02841, Republic of Korea*

**Byeonghak Park** − *School of Chemical Engineering, Sungkyunkwan University (SKKU), Suwon 16419, Republic of Korea*

**Yong Min Lee** − *Department of Semiconductor Systems Engineering, Korea University, Seoul 02841, Republic of Korea*

**Byung Ku Jung** − *Department of Materials Science and Engineering, Korea University, Seoul 02841, Republic of Korea*

**Sang Yeop Lee** − *Department of Materials Science and Engineering, Korea University, Seoul 02841, Republic of Korea*

**Jehyung Ok** − *School of Chemical Engineering, Sungkyunkwan University (SKKU), Suwon 16419, Republic of Korea*

**Bong Hoon Kim** − *Department of Robotics and Mechatronics Engineering, Daegu Gyeongbuk Institute of Science and Technology (DGIST), Daegu 42988, Republic of Korea;* orcid.org/0000-0002-4610-0176

**Tae-il Kim** − *School of Chemical Engineering, Sungkyunkwan University (SKKU), Suwon 16419, Republic of Korea; Biomedical Institute for Convergence at SKKU (BICS), Sungkyunkwan University (SKKU), Suwon 16419, Republic of Korea;* orcid.org/0000-0002-6667-5356

Complete contact information is available at: https://pubs.acs.org/10.1021/acsnano.2c02664


### Author Contributions

J.B. designed and performed the experiments. J.A., J.Z., T.H.K., B.P., Y.M.L., B.K.J., S.Y.L., J.O., B.H.K., and T-i.K. prepared the samples and collected the data. All authors discussed and interpreted the data. J.-I.C., C.H.L., and S.J.O. supervised the project. J.B., J.-I.C., C.H.L., and S.J.O. wrote the manuscript.

### Notes

The authors declare no competing financial interest.

## ACKNOWLEDGMENTS

This work was supported by a Basic Science Research Program through the National Research Foundation of Korea (NRF) funded by the Ministry of Science, ICT and Future Planning (Grant 2022R1A2C4001517), Creative Materials Discovery Program through the National Research Foundation of Korea (NRF) funded by Ministry of Science and ICT (Grant NRF-2018M3D1A1059001), National Research Foundation of Korea grant funded by the Korean government (Grant 2020M3H4A3081833), the National Research Foundation of Korea (NRF) grant funded by the Korean government (MSIT) (Grant No. 2021R1A2C2011325), and the National Research Foundation of Korea grant funded by the Korean government (Grant NRF-2018M3A7B4071110), Korea University Grant (Grants K2011261 and K2111871), the National Science Foundation (NSF) Chemical, Bioengineering, Envi-

ronment, and Transport Systems (CBET) (Award Number 2032529), and the Leslie A. Geddes Endowment at Purdue University.

## REFERENCES

(1) Chang, T.; Tanabe, Y.; Wojcik, C. C.; Barksdale, A. C.; Doshay, S.; Dong, Z.; Liu, H.; Zhang, M.; Chen, Y.; Su, Y.; Lee, T. H.; Ho, J. S.; Fan, J. A. A General Strategy for Stretchable Microwave Antenna Systems Using Serpentine Mesh Layouts. *Adv. Funct. Mater.* **2017**, *27*, 1703059.

(2) Fan, J. A.; Yeo, W. H.; Su, Y.; Hattori, Y.; Lee, W.; Jung, S. Y.; Zhang, Y.; Liu, Z.; Cheng, H.; Falgout, L.; Bajema, M.; Coleman, T.; Gregoire, D.; Larsen, R. J.; Huang, Y.; Rogers, J. A. Fractal Design Concepts for Stretchable Electronics. *Nat. Commun.* **2014**, *5*, 3266.

(3) Kim, Y. S.; Basir, A.; Herbert, R.; Kim, J.; Yoo, H.; Yeo, W. H. Soft Materials, Stretchable Mechanics, and Optimized Designs for Body-Wearable Compliant Antennas. *ACS Appl. Mater. Interfaces* **2020**, *12*, 3059−3067.

(4) Zhu, J.; Fox, J. J.; Yi, N.; Cheng, H. Structural Design for Stretchable Microstrip Antennas. *ACS Appl. Mater. Interfaces* **2019**, *11*, 8867−8877.

(5) Yao, S.; Myers, A.; Malhotra, A.; Lin, F.; Bozkurt, A.; Muth, J. F.; Zhu, Y. A Wearable Hydration Sensor with Conformal Nanowire Electrodes. *Adv. Healthc. Mater.* **2017**, *6*, 1601159.

(6) Helgason, R.; Banavali, A.; Lai, Y. Cohesive Dry ECG Sensor Using Silver Nanowires and PDMS Tuned for Adhesion. *Med. Devices Sensors* **2019**, *2*, e10025.

(7) Zhang, Y.; He, P.; Luo, M.; Xu, X.; Dai, G.; Yang, J. Highly Stretchable Polymer/Silver Nanowires Composite Sensor for Human Health Monitoring. *Nano Res.* **2020**, *13*, 919−926.

(8) Araki, T.; Uemura, T.; Yoshimoto, S.; Takemoto, A.; Noda, Y.; Izumi, S.; Sekitani, T. Wireless Monitoring Using a Stretchable and Transparent Sensor Sheet Containing Metal Nanowires. *Adv. Mater.* **2020**, *32*, 1902684.

(9) Kim, T.; Park, J.; Sohn, J.; Cho, D.; Jeon, S. Bioinspired, Highly Stretchable, and Conductive Dry Adhesives Based on 1D-2D Hybrid Carbon Nanocomposites for All-in-One ECG Electrodes. *ACS Nano* **2016**, *10*, 4770−4778.

(10) Cheng, Y.; Wang, R.; Zhai, H.; Sun, J. Stretchable Electronic Skin Based on Silver Nanowire Composite Fiber Electrodes for Sensing Pressure, Proximity, and Multidirectional Strain. *Nanoscale* **2017**, *9*, 3834−3842.

(11) Qiao, Y.; Wang, Y.; Jian, J.; Li, M.; Jiang, G.; Li, X.; Deng, G.; Ji, S.; Wei, Y.; Pang, Y.; Wu, Q.; Tian, H.; Yang, Y.; Wu, X.; Ren, T. L. Multifunctional and High-Performance Electronic Skin Based on Silver Nanowires Bridging Graphene. *Carbon N. Y.* **2020**, *156*, 253−260.

(12) Jung, D.; Lim, C.; Shim, H. J.; Kim, Y.; Park, C.; Jung, J.; Han, S. I.; Sunwoo, S. H.; Cho, K. W.; Cha, G. D.; Kim, D. C.; Koo, J. H.; Kim, J. H.; Hyeon, T.; Kim, D. H. Highly Conductive and Elastic Nanomembrane for Skin Electronics. *Science* **2021**, *373*, 1022−1026.

(13) Won, P.; Park, J. J.; Lee, T.; Ha, I.; Han, S.; Choi, M.; Lee, J.; Hong, S.; Cho, K. J.; Ko, S. H. Stretchable and Transparent Kirigami Conductor of Nanowire Percolation Network for Electronic Skin Applications. *Nano Lett.* **2019**, *19*, 6087−6096.

(14) Choi, T. Y.; Hwang, B. U.; Kim, B. Y.; Trung, T. Q.; Nam, Y. H.; Kim, D. N.; Eom, K.; Lee, N. E. Stretchable, Transparent, and Stretch-Unresponsive Capacitive Touch Sensor Array with Selectively Patterned Silver Nanowires/Reduced Graphene Oxide Electrodes. *ACS Appl. Mater. Interfaces* **2017**, *9*, 18022−18030.

(15) Kim, J. H.; Kim, S. R.; Kil, H. J.; Kim, Y. C.; Park, J. W. Highly Conformable, Transparent Electrodes for Epidermal Electronics. *Nano Lett.* **2018**, *18*, 4531−4540.

(16) Xu, Z.; Chen, L.; Lu, L.; Du, R.; Ma, W.; Cai, Y.; An, X.; Wu, H.; Luo, Q.; Xu, Q.; Zhang, Q.; Jia, X. A Highly-Adhesive and Self-Healing Elastomer for Bio-Interfacial Electrode. *Adv. Funct. Mater.* **2021**, *31*, 2006432.

(17) Lim, J. E.; Lee, S. M.; Kim, S. S.; Kim, T. W.; Koo, H. W.; Kim, H. K. Brush-Paintable and Highly Stretchable Ag Nanowire and PEDOT:PSS Hybrid Electrodes. *Sci. Rep.* **2017**, *7*, 14685.

(18) Choi, S.; Han, S. I.; Jung, D.; Hwang, H. J.; Lim, C.; Bae, S.; Park, O. K.; Tschabrunn, C. M.; Lee, M.; Bae, S. Y.; Yu, J. W.; Ryu, J. H.; Lee, S. W.; Park, K.; Kang, P. M.; Lee, W. B.; Nezafat, R.; Hyeon, T.; Kim, D. H. Highly Conductive, Stretchable and Biocompatible Ag−Au Core−Sheath Nanowire Composite for Wearable and Implantable Bioelectronics. *Nat. Nanotechnol.* **2018**, *13*, 1048−1056.

(19) Lee, M. S.; Lee, K.; Kim, S. Y.; Lee, H.; Park, J.; Choi, K. H.; Kim, H. K.; Kim, D. G.; Lee, D. Y.; Nam, S.; Park, J. U. High-Performance, Transparent, and Stretchable Electrodes Using Graphene-Metal Nanowire Hybrid Structures. *Nano Lett.* **2013**, *13*, 2814−2821.

(20) Liang, J.; Li, L.; Tong, K.; Ren, Z.; Hu, W.; Niu, X.; Chen, Y.; Pei, Q. Silver Nanowire Percolation Network Soldered with Graphene Oxide at Room Temperature and Its Application for Fully Stretchable Polymer Light-Emitting Diodes. *ACS Nano* **2014**, *8*, 1590−1600.

(21) Kim, D. H.; Ghaffari, R.; Lu, N.; Rogers, J. A. Flexible and Stretchable Electronics for Biointegrated Devices. *Annu. Rev. Biomed. Eng.* **2012**, *14*, 113−128.

(22) Wang, S.; Wang, Z.; Huang, Y.; Hu, Y.; Yuan, L.; Guo, S.; Zheng, L.; Chen, M.; Yang, C.; Zheng, Y.; Qi, J.; Yu, L.; Li, H.; Wang, W.; Ji, D.; Chen, X.; Li, J.; Li, L.; Hu, W. Directly Patterning Conductive Polymer Electrodes on Organic Semiconductor *via in Situ* Polymerization in Microchannels for High-Performance Organic Transistors. *ACS Appl. Mater. Interfaces* **2021**, *13*, 17852−17860.

(23) Guo, W.; Zheng, P.; Huang, X.; Zhuo, H.; Wu, Y.; Yin, Z.; Li, Z.; Wu, H. Matrix-Independent Highly Conductive Composites for Electrodes and Interconnects in Stretchable Electronics. *ACS Appl. Mater. Interfaces* **2019**, *11*, 8567−8575.

(24) Xu, F.; Zhu, Y. Highly Conductive and Stretchable Silver Nanowire Conductors. *Adv. Mater.* **2012**, *24*, 5117−5122.

(25) Seo, J. W.; Kim, K.; Seo, K. W.; Kim, M. K.; Jeong, S.; Kim, H.; Ghim, J. W.; Lee, J. H.; Choi, N.; Lee, J. Y.; Lee, H. J. Artifact-Free 2D Mapping of Neural Activity *In Vivo* through Transparent Gold Nanonetwork Array. *Adv. Funct. Mater.* **2020**, *30*, 2000896.

(26) Lee, P.; Lee, J.; Lee, H.; Yeo, J.; Hong, S.; Nam, K. H.; Lee, D.; Lee, S. S.; Ko, S. H. Highly Stretchable and Highly Conductive Metal Electrode by Very Long Metal Nanowire Percolation Network. *Adv. Mater.* **2012**, *24*, 3326−3332.

(27) Jiang, Z.; Nayeem, M. O. G.; Fukuda, K.; Ding, S.; Jin, H.; Yokota, T.; Inoue, D.; Hashizume, D.; Someya, T. Highly Stretchable Metallic Nanowire Networks Reinforced by the Underlying Randomly Distributed Elastic Polymer Nanofibers *via* Interfacial Adhesion Improvement. *Adv. Mater.* **2019**, *31* (37), 1903446.

(28) Qi, D.; Liu, Z.; Yu, M.; Liu, Y.; Tang, Y.; Lv, J.; Li, Y.; Wei, J.; Liedberg, B.; Yu, Z.; Chen, X. Highly Stretchable Gold Nanobelts with Sinusoidal Structures for Recording Electrocorticograms. *Adv. Mater.* **2015**, *27*, 3145−3151.

(29) Yan, Z.; Pan, T.; Xue, M.; Chen, C.; Cui, Y.; Yao, G.; Huang, L.; Liao, F.; Jing, W.; Zhang, H.; Gao, M.; Guo, D.; Xia, Y.; Lin, Y. Thermal Release Transfer Printing for Stretchable Conformal Bioelectronics. *Adv. Sci.* **2017**, *4*, 1700251.

(30) Lee, W.; Kim, D.; Matsuhisa, N.; Nagase, M.; Sekino, M.; Malliaras, G. G.; Yokota, T.; Someya, T. Transparent, Conformable, Active Multielectrode Array Using Organic Electrochemical Transistors. *Proc. Natl. Acad. Sci. U. S. A.* **2017**, *114*, 10554−10559.

(31) Cui, Z.; Han, Y.; Huang, Q.; Dong, J.; Zhu, Y. Electrohydrodynamic Printing of Silver Nanowires for Flexible and Stretchable Electronics. *Nanoscale* **2018**, *10*, 6806−6811.

(32) Rabczuk, T.; Belytschko, T. Application of Particle Methods to Static Fracture of Reinforced Concrete Structures. *Int. J. Fract.* **2006**, *137*, 19−49.

(33) Raki, L.; Beaudoin, J.; Alizadeh, R.; Makar, J.; Sato, T. Cement and Concrete Nanoscience and Nanotechnology. *Materials (Basel)* **2010**, *3*, 918−942.

(34) Kim, S. O.; Han, C. J.; Lee, C. R.; Kim, J. W. Highly Transparent, Stretchable, and Conformable Silicone-Based Strain/



https://doi.org/10.1021/acsnano.2c02664
*ACS Nano* 2022, 16, 12134−12144

Pressure-Sensitive Capacitor Using Adhesive Polydimethylsiloxane. *J. Alloys Compd.* **2020**, *841*, 155773.
(35) Hwang, Y.; Hwang, Y. H.; Choi, K. W.; Lee, S.; Kim, S.; Park, S. J.; Ju, B. K. Highly Stabilized Flexible Transparent Capacitive Photodetector Based on Silver Nanowire/Graphene Hybrid Electrodes. *Sci. Rep.* **2021**, *11*, 10499.
(36) Yoo, J.; Jeong, S.; Kim, S.; Je, J. H. A Stretchable Nanowire UV-Vis-NIR Photodetector with High Performance. *Adv. Mater.* **2015**, *27*, 1712−1717.
(37) Yan, C.; Wang, J.; Wang, X.; Kang, W.; Cui, M.; Foo, C. Y.; Lee, P. S. An Intrinsically Stretchable Nanowire Photodetector with a Fully Embedded Structure. *Adv. Mater.* **2014**, *26*, 943−950.
(38) Kim, H.; Lee, S. W.; Joh, H.; Seong, M.; Lee, W. S.; Kang, M. S.; Pyo, J. B.; Oh, S. J. Chemically Designed Metallic/Insulating Hybrid Nanostructures with Silver Nanocrystals for Highly Sensitive Wearable Pressure Sensors. *ACS Appl. Mater. Interfaces* **2018**, *10*, 1389−1398.
(39) Bang, J.; Lee, W. S.; Park, B.; Joh, H.; Woo, H. K.; Jeon, S.; Ahn, J.; Jeong, C.; Kim, T.-i.; Oh, S. J. Highly Sensitive Temperature Sensor: Ligand-Treated Ag Nanocrystal Thin Films on PDMS with Thermal Expansion Strategy. *Adv. Funct. Mater.* **2019**, *29*, 1903047.
(40) Hemmilä, S.; Cauich-Rodríguez, J. V.; Kreutzer, J.; Kallio, P. Rapid, Simple, and Cost-Effective Treatments to Achieve Long-Term Hydrophilic PDMS Surfaces. *Appl. Surf. Sci.* **2012**, *258* (24), 9864−9875.
(41) Ranjan, P.; Agrawal, S.; Sinha, A.; Rao, T. R.; Balakrishnan, J.; Thakur, A. D. A Low-Cost Non-Explosive Synthesis of Graphene Oxide for Scalable Applications. *Sci. Rep.* **2018**, *8*, 12007.
(42) Huang, Y. L.; Tien, H. W.; Ma, C. C. M.; Yang, S. Y.; Wu, S. Y.; Liu, H. Y.; Mai, Y. W. Effect of Extended Polymer Chains on Properties of Transparent Graphene Nanosheets Conductive Film. *J. Mater. Chem.* **2011**, *21*, 18236−18241.
(43) Zhidkov, I. S.; Kurmaev, E. Z.; Condorelli, M.; Cholakh, S. O.; Boyarchenkov, A. S.; Fazio, E.; D'urso, L. X-Ray Photoelectron Spectra of Ag-Au Colloidal Nanoparticles after Interaction with Linear Carbon Chains. *Appl. Sci.* **2021**, *11*, 685.
(44) Mao, H.; Feng, J.; Ma, X.; Wu, C.; Zhao, X. One-Dimensional Silver Nanowires Synthesized by Self-Seeding Polyol Process. *J. Nanoparticle Res.* **2012**, *14*, 887.
(45) Wang, G. H.; Zhu, J. J.; Kan, C. X.; Wan, J. G.; Han, M. High-Yield Synthesis of Uniform Ag Nanowires with High Aspect Ratios by Introducing the Long-Chain PVP in an Improved Polyol Process. *J. Nanomater.* **2011**, *2011*, 982547.
(46) Ma, J.; Zhan, M. Rapid Production of Silver Nanowires Based on High Concentration of AgNO3 Precursor and Use of FeCl3 as Reaction Promoter. *RSC Adv.* **2014**, *4*, 21060−21071.
(47) Sim, H.; Kim, C.; Bok, S.; Kim, M. K.; Oh, H.; Lim, G. H.; Cho, S. M.; Lim, B. Five-Minute Synthesis of Silver Nanowires and Their Roll-to-Roll Processing for Large-Area Organic Light Emitting Diodes. *Nanoscale* **2018**, *10*, 12087−12092.
(48) Lee, W.; Kobayashi, S.; Nagase, M.; Jimbo, Y.; Saito, I.; Inoue, Y.; Yambe, T.; Sekino, M.; Malliaras, G. G.; Yokota, T.; Tanaka, M.; Someya, T. Nonthrombogenic, Stretchable, Active Multielectrode Array for Electroanatomical Mapping. *Sci. Adv.* **2018**, *4*, eaau2426.
(49) Chang, T.; Tanabe, Y.; Wojcik, C. C.; Barksdale, A. C.; Doshay, S.; Dong, Z.; Liu, H.; Zhang, M.; Chen, Y.; Su, Y.; Lee, T. H.; Ho, J. S.; Fan, J. A. A General Strategy for Stretchable Microwave Antenna Systems Using Serpentine Mesh Layouts. *Adv. Funct. Mater.* **2017**, *27*, 1703059.
(50) Li, X.; Zhao, Y. B.; Fan, F.; Levina, L.; Liu, M.; Quintero-Bermudez, R.; Gong, X.; Quan, L. N.; Fan, J.; Yang, Z.; Hoogland, S.; Voznyy, O.; Lu, Z. H.; Sargent, E. H. Bright Colloidal Quantum Dot Light-Emitting Diodes Enabled by Efficient Chlorination. *Nat. Photonics* **2018**, *12*, 159−164.
(51) Fu, Y.; Kim, D.; Jiang, W.; Yin, W.; Ahn, T. K.; Chae, H. Excellent Stability of Thicker Shell CdSe@ZnS/ZnS Quantum Dots. *RSC Adv.* **2017**, *7*, 40866−40872.
(52) Lee, K.; Han, C.; Kang, H.; Ko, H.; Lee, C.; Lee, J.; Myoung, N.; Yim, S.; Yang, H. Highly Efficient, Color-Reproducible Full-Color Electroluminescent Devices Based on Red/Green/Blue Quantum Dot-Mixed Multilayer. *ACS Nano* **2015**, *9*, 10941−10949.




https://doi.org/10.1021/acsnano.2c02664
*ACS Nano* 2022, 16, 12134−12144